Electronic structure of the martensitic phases B19'-NiTi and B19-PdTi

Electronic structure of the martensitic phases B19'-NiTi and B19-PdTi

G Bihlmayer, R Eibler and A Neckel

Institute of Physical Chemistry, University of Vienna, Währingerstraße 42, A-1090 Vienna, Austria

Abstract. Self-consistent LAPW band structure calculations were performed for the martensitic phases B19'-NiTi and B19-PdTi. The resulting densities of states (DOS), partial charges, partial densities of states, electron densities and Fermi surfaces were compared to the results of a former calculation for B2-NiTi and B2-PdTi. The DOS at the Fermi level is lower for the martensitic than for the austenitic phases. The most significant changes at the phase transition were found for the Fermi surfaces and derived properties. Nesting between electron and hole sheets of the Fermi surface is greatly reduced in the martensites. The generalized susceptibility and the function $\zeta(q)$ approximating the electron–phonon contribution to the dynamical matrix were also calculated for three symmetry directions. Maxima of $\zeta(q)$ show up only in the [111] direction. Furthermore, calculated XPS spectra and optical conductivities were compared to experiment, if available.

1. Introduction

NiTi crystallizes at low temperatures in a monoclinic structure (B19'-NiTi) [1] which, on heating above 333 K, transforms directly to the cubic austenitic B2 phase [2]. On cooling B2-NiTi below the martensitic transformation temperature M_s of 333 K [3], the system undergoes a phase transition to the martensitic phase (B19'), involving several intermediate phases [4–6]. The phase transition is also accompanied by the so-called shape-memory effect [2] widely used in industry and medicine. The less well known PdTi system also undergoes a martensitic phase transition to the low-temperature orthorhombic B19 phase [7]; however, it does so at the much higher temperature of $\approx$ 790 K [8, 9] and without formation of intermediate phases.

Figure 1 shows how the low-temperature phases can be formed from the high-temperature B2 structure. One starts by constructing a unit cell twice as large as the cubic unit cell inscribed into four cubic unit cells. We rotate the new cell by $\pi/4$ around the $[001]_{B2}$ axis and shift it by $a/2$ in the $[001]_{B2}$ direction (top right). In the case of NiTi, this cell is tilted backwards in the $[110]_{B2}$ direction, the Ni atoms are shifted in the $[111]_{B2}$ and $[1\bar{1}\bar{1}]_{B2}$ and the Ti atoms in the $[\bar{1}\bar{1}1]_{B2}$ and $[11\bar{1}]_{B2}$ directions and, finally, the B19' structure is obtained by a monoclinic distortion. For the orthorhombic structure of B19-PdTi, both the Pd and Ti atoms are shifted in the $[110]_{B2}$ and $[1\bar{1}0]_{B2}$ directions and the monoclinic distortion does not take place. The unit cells of B19'-NiTi and B19-PdTi accommodate both two formula units of NiTi (PdTi).

Several attempts [10–17] have been made to explain the occurrence of the martensitic phase transformation of NiTi by special features of the band structure of the B2 phase showing up in the density of states (DOS) [3, 10] and/or the Fermi surface [11–16] and
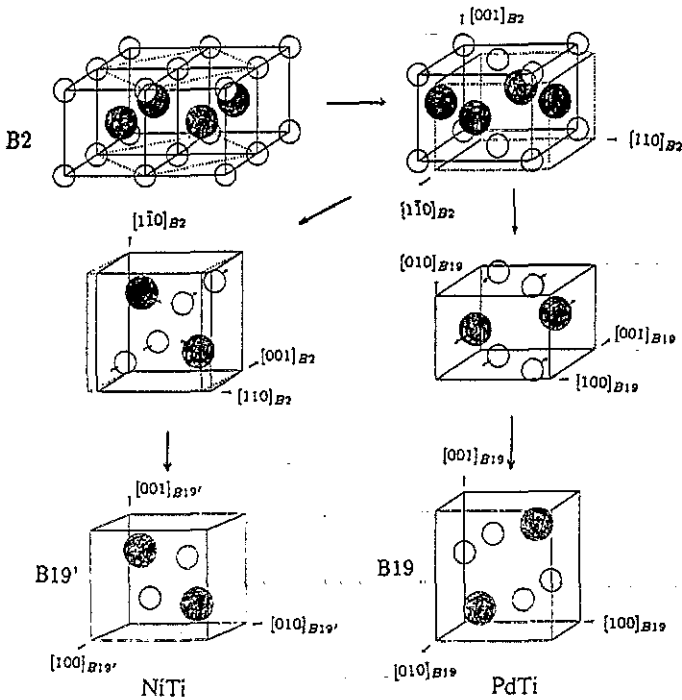
Figure 1. Formation of B19'-NiTi (left) and B19-PdTi (right) from the B2-phases. Full circles: Ti atoms; open circles: Ni(Pd) atoms.

leading, possibly by the formation of charge density waves (CDW) [18], to a softening of particular branches of the phonon spectra either in the [111] or [110] direction [5]. The reverse transformation from martensite to austenite, by heating the B19' (B19) phase, is less well investigated.

Whereas several band structure calculations are available for B2-NiTi [14–17, 19–24] and, to a lesser extent, for B2-PdTi [17, 24, 25], only one has been published for B19'-NiTi [26] until now. We have already published LAPW band structure calculations for B2-NiTi and B2-PdTi [27]. From accurate calculations of the Fermi surfaces, we calculated the generalized susceptibility of non-interacting electrons $\chi_0(q)$ and an approximate expression $\zeta(q)$ for the electron–phonon coupling contribution to the dynamical matrix of phonons in several crystallographic directions of B2-NiTi and B2-PdTi. We arrived thereby at a quantitative estimate of the influence of nesting regions of the Fermi surface on the electron–phonon interaction. Maxima of $\chi_0(q)$ and $\zeta(q)$ were found for NiTi for a phonon q of $[0.31, 0.31, 0]2\pi/a$, thus very near the commensurate position of $[\frac{1}{3}, \frac{1}{3}, 0]2\pi/a$. Thereby, one can explain the softening of an acoustic phonon of this q value, enabling the formation of an intermediate commensurate superstructure R [4, 5] during the martensitic phase transition from B2-NiTi to B19'-NiTi. For PdTi, the maximum lies at the more incommensurate position of $[0.28, 0.28, 0]2\pi/a$. Indeed, no commensurate superstructure R is formed during the martensitic phase transition of PdTi. However, by adding 5% Fe, the Fermi level is shifted and the Fermi surface changed in such a way that a related intermediate commensurate phase is formed upon cooling of B2-PdTi [28]. In stoichiometric PdTi, the Fermi surface shows necks in the [110] directions at 0 K rendering nesting of hole and electron surfaces less effective, at least in the (001) planes. At higher temperatures increased nesting is possible because the Fermi surface is smeared. Thus, one can explain the higher martensitic transformation temperature of the Pd alloy.

In this paper we present band structure data for the low-temperature phases B19'- NiTi

and B19-PdTi, such as band structures, densities of states (DOS), partial local DOS and Fermi surfaces. Furthermore, in order to shed light on the transformation behaviour of both alloys, we will discuss the generalized susceptibility and $\zeta(q)$ curves for both the high- and low-temperature phases in several crystallographic directions in more detail. Calculated XPS spectra and optical conductivities are compared to experiment, if available. Energetic aspects necessitating full-potential calculations will be treated in a third paper [29].

2. Procedure

We used the scalar-relativistic self-consistent LAPW method [30] with the Vashishta–Singwi Hedin–Lundqvist exchange-correlation potential [31]. The Ti and Ni 3s and 3p (Pd 4s and 4p) states were treated as band states in a separate energy window. The geometric parameters for the B19' structure of martensitic NiTi and for the B19 structure of martensitic PdTi [32] are displayed together with the muffin-tin radii in table 1. The core states were treated fully relativistically in the frozen-core approximation. We used a potential of muffin-tin type, but a warped electron density in the interstitial region, described by a Fourier series with 350 coefficients for B19'-NiTi and 200 for B19-PdTi. The l expansion was extended to a maximal value l_{max} of 12.

Table 1. Geometry parameters and muffin-tin radii used for the calculations.

B19' NiTi	Hermann-Mauguin: $P11(2_1/m)$			
Lattice constants	$a = 2.885\,\text{Å}$ i.e. 5.452 au			
	$b = 4.622\,\text{Å}$ i.e. 8.734 au			
	$c = 4.120\,\text{Å}$ i.e. 7.786 au			
	$\gamma = 96.8°$			
Ni	$(x, y, \frac{1}{4}), (\bar{x}, \bar{y}, \frac{3}{4})$	$x = 0.0525$	$y = 0.193$	$R_{MT} = 2.2636\,\text{au}$
Ti	$(x, y, \frac{3}{4}), (\bar{x}, \bar{y}, \frac{1}{4})$	$x = 0.5247$	$y = 0.279$	$R_{MT} = 2.4226\,\text{au}$
B19 PdTi	Hermann-Mauguin: $Pmma$			
Lattice constants	$a = 4.56\,\text{Å}$ i.e. 8.617 au			
	$b = 2.81\,\text{Å}$ i.e. 5.310 au			
	$c = 4.89\,\text{Å}$ i.e. 9.241 au			
Pd	$(\frac{1}{4}, 0, x), (\frac{3}{4}, 0, \bar{x})$	$x = 0.68$	$R_{MT} = 2.6779\,\text{au}$	
Ti	$(\frac{1}{4}, \frac{1}{2}, x), (\frac{3}{4}, \frac{1}{2}, \bar{x})$	$x = 0.18$	$R_{MT} = 2.5457\,\text{au}$	

Expanding the wavefunction in augmented plane waves, between 240 and 260 plane waves for B19'-NiTi and between 205 and 215 plane waves for B19-PdTi—corresponding to a RKM value of eight—were taken into account, with RKM being the product of the largest reciprocal lattice vector in the sum and the average muffin-tin radius. The doubling of the size of the plane-wave basis caused relative shifts of the eigenvalues less than 0.15 mRyd.

In order to obtain well converged results we had to perform 110 iterations for B19'-NiTi and 100 iterations for B19-PdTi.

Most of the iterations were performed with a mesh of 104 k points for B19'-NiTi and of 80 k points for B19-PdTi in the irreducible wedge of the Brillouin zone. In the last iterations, eigenvalues and wavefunctions were calculated for a mesh of 330 (NiTi) and 225 (PdTi) k points corresponding to a total of 1024 k points in the entire Brillouin zone. With these eigenvalues the band structures, densities of states and partial local DOS were

calculated. A finer mesh of 2601 (1377) non-equivalent k points corresponding to 8192 k points in the whole Brillouin zone was employed for the calculation of the Fermi surface plots.

3. Results

3.1. Band structure, densities of state and XPS spectra

Figure 2 shows the band structures of B19'-NiTi (*a*) and B19-PdTi (*b*) for several symmetry directions in k space. The notation of the k points was chosen according to Bradley and Cracknell [33] with γ as monoclinic angle. A comparison with the band structures of the B2 phases [27] shows twice as many bands because of the larger unit cell. In the interior of the Brillouin zone, the lower symmetry of the low-temperature structures leads to a splitting of degenerate bands. However, bands can stick together in some directions on the surface of the Brillouin zone due to time-reversal degeneracy [34], as for example in the X–U and S–R direction of B19-PdTi and the C–Z–D and E–Z direction of B19'-NiTi. When band structures for crystals of different symmetry are compared, only equivalent symmetry directions should be considered. For example, the Γ–X direction of orthorhombic B19-PdTi corresponds to the Γ–Z direction of monoclinic B19'-NiTi. In contrast to the B2 phases, the three $[110]_{B2}$ directions are no longer equivalent in the low-temperature phases.
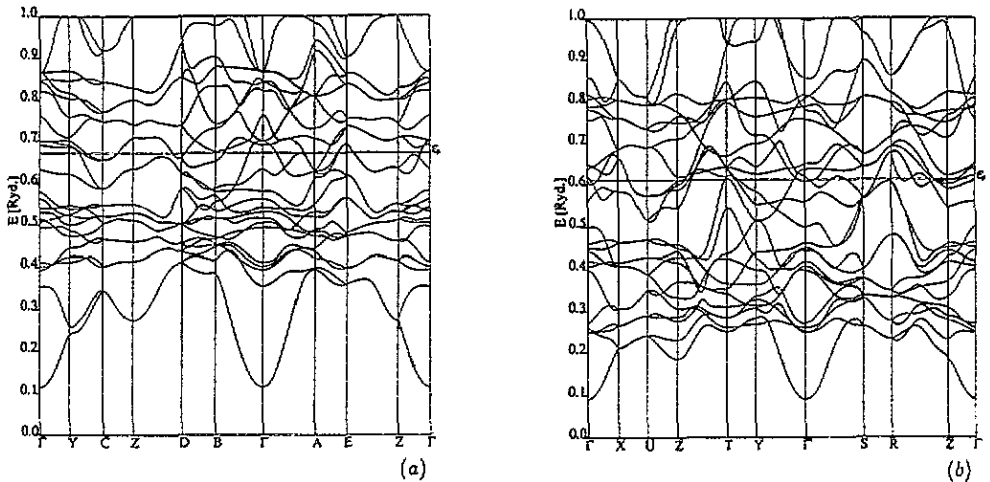

Figure 2. Band structures of B19'-NiTi (*a*) and B19-PdTi (*b*).

Until now, only one band structure has been published for B19'-NiTi [26] which was calculated by means of the LMTO–ASA method. The occupied bandwidth for both NiTi phases is only higher by 0.15 eV in [26] than in the present calculation and scarcely changes upon the phase transformation as can be deduced from table 1 of [26]. The B19'-NiTi band structure looks quite similar in both calculations in the lower part of the occupied bands, but larger differences can be detected at higher energies and especially near the Fermi level, which should also lead to corresponding differences in the DOS and Fermi surfaces. For example, there exists a very flat band in the direction Z_c–M_c, just below E_F, in [26], whereas in the present calculation a flat band in the corresponding Z–E direction is only found near Z, because the seventh and eighth band at M_c are situated below E_F in figure 2 of [26], but
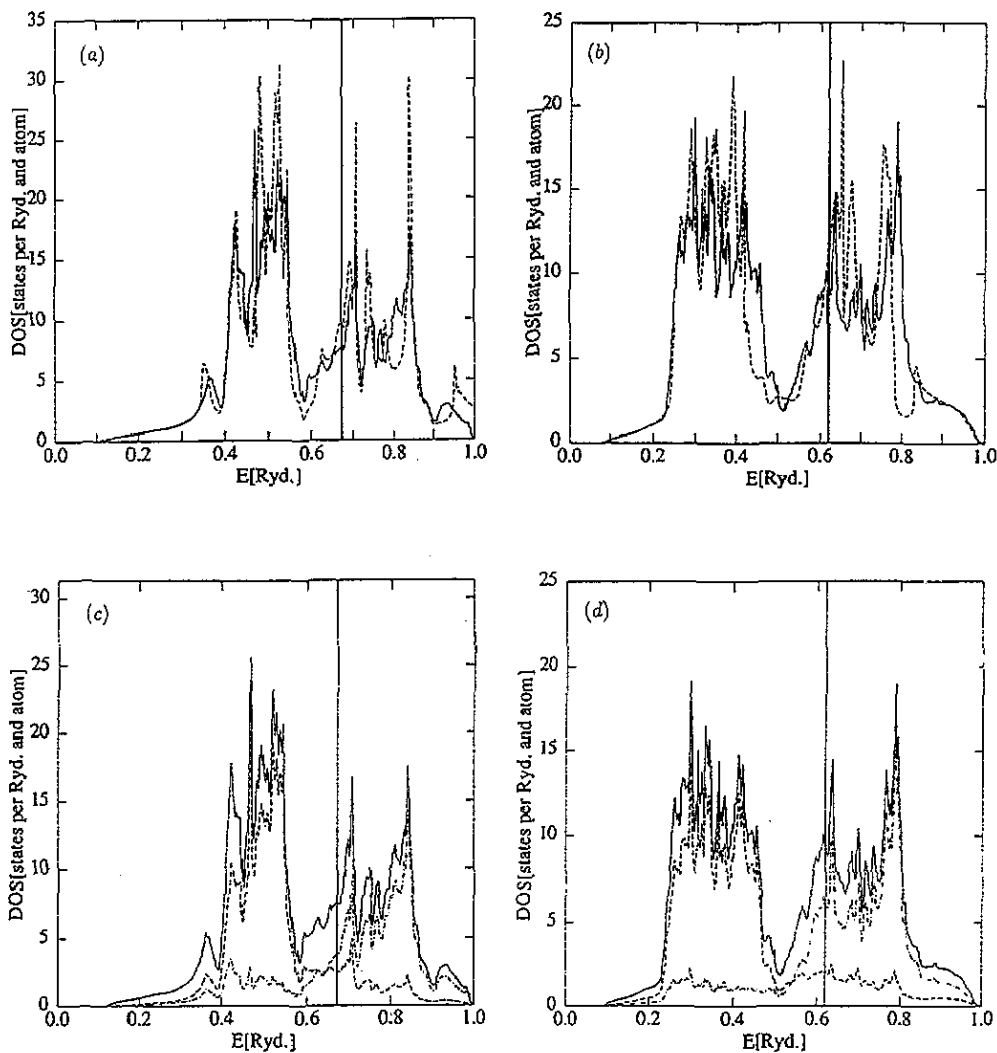
Figure 3. Densities of states (DOS) in states (one spin direction) per Ryd and atom for B2-NiTi (dotted curve) and B19'-NiTi (full curve) (*a*), B2-PdTi (dotted curve) and B19-PdTi (full curve) (*b*), DOS (full curve) and local Ni(Pd) DOS (broken curve) and Ti DOS (chain curve) for B19'-NiTi (*c*) and B19-PdTi (*d*).

above E_F at the corresponding k vector E in the present work. Also, it seems that the band structure of [26] was plotted without properly taking into account the non-crossing rules.

We calculated the DOS and partial local DOS by means of the tetrahedron method [35]. Figure 3 shows the total DOS of both B2-NiTi and B19'-NiTi (*a*) and B2-PdTi and B19-PdTi (*b*) as well as the partial local DOS for B19'-NiTi (*c*) and B19-PdTi (*d*). The DOS are very similar for both the austenitic and martensitic phases. Because of the lower symmetry of the low-temperature phases, which removes the degeneracy of bands, the DOS of the low-temperature phases shows more structure and peaks of smaller intensity than found for B2-NiTi and B2-PdTi. In agreement with [26], the bandwidths of both NiTi phases are very similar. Summing over subband A (s band + Ni d subband up to the sharp minimum in the DOS between 0.5 and 0.6 Ryd) and subband B (occupied part of the Ti d band from this minimum to the Fermi level) the bandwidth of all occupied states is 0.1 eV narrower in

B19'-NiTi than in B2-NiTi. Subband A is 0.7 eV narrower in B19-PdTi than in B19'-NiTi, and subband B 0.2 eV larger (see table 2). For both systems, the DOS at the Fermi level is lower for the martensitic phases and E_F lies in the ascent of the second DOS peak dominated by Ti d states, for B19'-NiTi in a distinct shoulder.

Table 2. Bandwidths of B2-NiTi and B19'-NiTi, B2-PdTi and B19-PdTi, in eV.

Bandwidth	B2-NiTi	B19'-NiTi	B2-PdTi	B19-PdTi
s + Ni(Pd) d band (subband A)	6.5	6.4	5.7	5.7
Occupied Ti d band (subband B)	1.3	1.2	1.6	1.4
All occupied bands	7.8	7.6	7.3	7.2
Ti d band	4.3	4.3	4.1	4.8

In table 3, the Fermi energy and the partial local DOS at E_F are displayed for B19-PdTi and B19'-NiTi. Compared to the values for the cubic phases [27] and taking into account that the DOS values are given in units of states (one spin direction) per Ryd and cell (thus for one formula unit of XTi (X = Ni, Pd) for the B2 phases and for two formula units of XTi for the martensitic phases), the DOS at E_F is 20% lower for the martensitic than for the cubic phases and the percentage of the partial local Ti DOS higher. The DOS decrease can be mainly ascribed to a decrease of the Ni DOS. Mixing between Ti and (Ni, Pd) states is reduced in the martensitic phases compared to the austenitic phases, in good agreement with conclusions from experiment [12].

Table 3. DOS at the Fermi level (states per Ryd and cell).

Alloy	g^{tot}	$g^{Ni,Pd}$	g^{Ti}	$g^{(Ni,Pd)p}$	$g^{Ti\,p}$	$g^{(Ni,Pd)d}$	$g^{Ti\,d}$	Fermi energy
B19'-NiTi	30.32	10.23	15.25	1.56	0.70	8.16	14.27	0.6707 Ryd
B19-PdTi	38.75	8.51	25.13	2.98	1.01	5.02	23.01	0.6188 Ryd

The partial local s (p) DOS is very small in all compounds compared to the d DOS. The phase transition is not accompanied by a shift of the free-electron (s and p) DOS relative to the d DOS, as was postulated by Mitchell and co-workers [10] to be the first step leading to the martensitic phase transformation. The lower DOS at E_F for B19'-NiTi is also confirmed by the temperature-dependence of the electrical resistance $\rho(T)$ and the magnetic susceptibility $\chi(T)$ [36].

The band structure of B19'-NiTi published in [26] differs considerably from the band structure of B2-NiTi near E_F and, thus, a peak in the minimum between the Ni-dominated and the Ti-dominated DOS peaks emerges filling the minimum. According to Kulkova and co-workers [26], the Fermi level of B19'-NiTi lies exactly in this peak, whereas in the present calculation no such peak can be detected and, in agreement with experiment, the DOS of B19'-NiTi is only slightly different from the DOS of B2-NiTi. Also, almost no difference was found between the XPS spectra of the both NiTi phases [36].

Figure 4 shows the calculated XPS spectra of B2-NiTi and B19'-NiTi and B2-PdTi and B19-PdTi. For B2-NiTi and B19-PdTi, recently measured spectra [24] are also shown as dotted curves. The spectra were calculated as described in more detail in [23] by weighting the partial local DOS with photoabsorption cross sections determined by means of a multiple-scattering formalism employing a LEED function for the final state of the emitted photoelectron [37]. For NiTi, self-energy effects are supposed to be high due to the highly correlated Ni d electrons [38]. As in [23], we simulated the real part of the 'self-energy'

correction for the states $E_n(k)$ of B2-NiTi and B19'-NiTi by shifting each eigenvalue by $0.3(E_n(k) - E_F)q_{3d}^{Ni}$. Hereby, q_{3d}^{Ni} is the partial local Ni 3d charge in the Ni sphere. For PdTi, self-energy effects are less well investigated and supposed to be smaller. Therefore, the eigenvalues were not shifted.

The calculated spectra were smeared with a spectrometer function of half-width 0.6 eV and the imaginary part of the complex self-energy was approximated by lifetime broadening the XPS spectra with a Lorentzian of half-width 1.0 eV as in [23].

The calculated spectrum of B2-NiTi agrees very well with experiment [24]. Only the satellite at 7.2 eV, corresponding to a final state of two correlated 3d holes, cannot be reproduced by a calculation based solely on one-electron states. The XPS spectra for B2-NiTi and B19'-NiTi are very similar.

The shape and width of the XPS peaks are well reproduced for B19-PdTi, but all calculated peaks are shifted by about 0.5 eV to lower binding energies. The calculated XPS of B19-PdTi shows a broad double-peak of width 3 eV with maxima at 3 and 4.2 eV instead of one narrower peak of width 2.5 eV at 3.7 eV as for B2-PdTi. The relative intensity of the small peak at 0.5 eV is reduced in intensity for B19-PdTi compared to B2-PdTi.

Table 4. Partial charges in the subbands.

	Alloy	Ni (Pd) sphere			
		s	p	d	Tot
Total	B19'-NiTi	0.991	0.763	16.46	18.24
	B19-PdTi	1.175	1.057	16.73	19.09
Subband A	B19'-NiTi	0.896	0.482	15.06	16.45
	B19-PdTi	0.985	0.518	15.55	17.11
Subband B	B19'-NiTi	0.095	0.281	1.405	1.790
	B19-PdTi	0.190	0.539	0.185	1.950

	Alloy	Ti sphere				
		s	p	d	Tot	q_{out}
Total	B19'-NiTi	0.546	0.562	3.880	5.057	4.700
	B19-PdTi	0.634	0.625	4.079	5.429	3.513
Subband A	B19'-NiTi	0.507	0.444	2.385	3.395	3.951
	B19-PdTi	0.540	0.439	1.517	2.567	2.621
Subband B	B19'-NiTi	0.039	0.118	1.495	1.662	0.748
	B19-PdTi	0.094	0.186	2.562	2.862	0.892

It was deduced from the T dependence of the magnetic susceptibility [36] that the Fermi level should lie in or near a DOS minimum for B19'-NiTi and in or near a DOS maximum for B2-NiTi. However, more recent measurements of the magnetic susceptibility of NiTi powders do not confirm the positive slope of the $\chi(T)$ curve for the low-temperature phase region and the negative slope of $\chi(T)$ for the high-temperature B2-phase region [39]. From measurements of the T dependence of the thermoelectric power and the electrical resistivity, the authors of [39] conclude that the DOS at E_F should remain almost constant for the two NiTi phases. The lower magnetic susceptibility of B19'-NiTi is explained in [39] by its higher Debye temperature. Thus, the crystal should get softer on heating above the austenitic transition temperature.

Table 4 shows the partial local charges in the subbands A and B of B19'-NiTi and B19-PdTi to be compared with the partial local charges of B2-PdTi and B2-NiTi from [27]. The definition of the subbands A and B was given earlier. The higher localization of the d

states produces a higher percentage of Ni(Pd) d-like charge in subband A and of Ti d-like charge in subband B in the low-temperature martensitic phases.
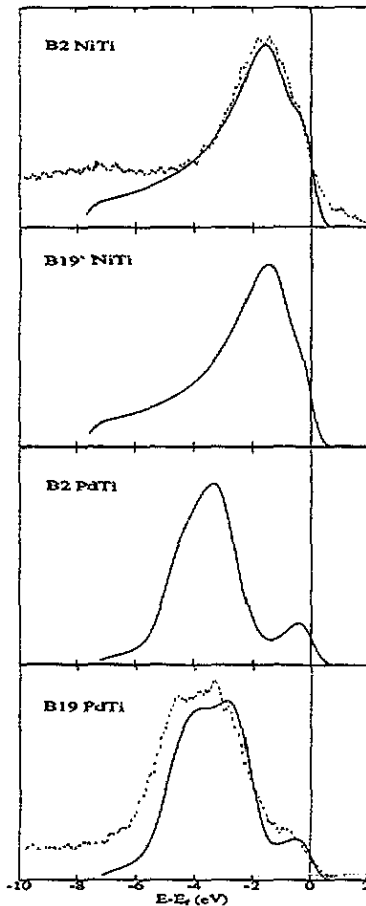

Figure 4. Calculated XPS spectra for B2-NiTi and B19'-NiTi, B2-PdTi and B19-PdTi in arbitrary units. For B2-NiTi and B19-PdTi the experimental XPS of [24] is also shown (dotted curve).
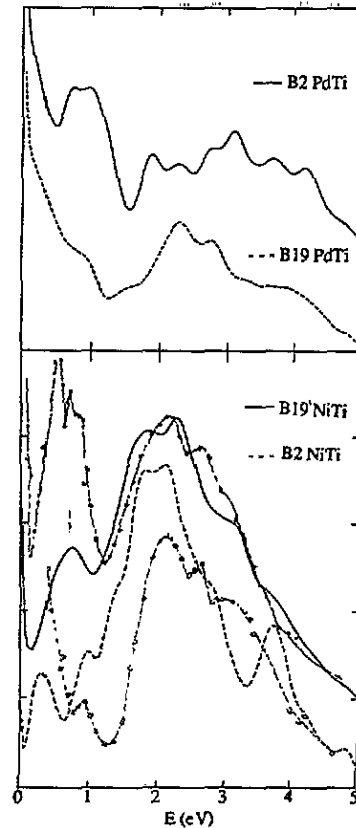
Figure 5. Optical conductivities in arbitrary units for B2-PdTi and B19-PdTi (top), B2-NiTi and B19'-NiTi (bottom). Measured optical conductivities [36] of B2-NiTi (empty circles) and B19'-NiTi (full circles) are also shown.

3.2. Optical conductivity

The optical conductivities for B2-NiTi and B19'-NiTi have been measured in [40]. In the visible region of the spectra, from 1.2 to 4.9 eV, a broad peak is found for both phases which is obviously not much affected by the martensitic transformation. However, it should be noted that the absorption edge for B2-NiTi is much steeper and the high energy part of the band is slightly narrowed. Furthermore, the IR part of the spectrum changes drastically as a result of the martensitic transformation. For the austenitic B2-NiTi, the conductivity rises continuously on reduction of the photon energy below 1.2 eV, with several peaks at very low energies (1.0, 0.35, 0.24, 0.17, 0.113 and 0.085 eV). For the martensite, only a shoulder at 0.17 eV can be detected at very low energies, but a new peak emerges between

0.2 and 1.2 eV. The steep rise of the optical conductivity below 0.2 eV can be ascribed to the contribution of free carriers.

The optical conductivity has not been measured for B2-PdTi and B19-PdTi.

The k selection rule is known to be valid for optical transitions [41]. The interband contribution to the optical conductivity can therefore be approximated by

$$\sigma(\omega) \propto \frac{1}{\omega} \sum_i \sum_j \int_{BZ} \delta[E_j(k) - E_i(k) - \hbar\omega][1 - f(E_j(k))] f(E_i(k)) d^3 k$$

if all transition moments are assumed to be constant. As ensured by the Fermi factors $f(E)$, the sum over i runs over all occupied and the sum over j over all unoccupied states; ω is the frequency of the absorbed light. Thus, $\sigma(\omega)$ is proportional to the so-called restricted joint density of states JDOS. As for the XPS spectra, self-energy effects should be taken into account. The eigenvalues of B2-NiTi and B19'-NiTi were shifted as has been described for the calculation of the XPS spectra. Furthermore, lifetime broadening of width 0.1 eV was applied to all four optical conductivity curves.

In figure 5, the calculated optical conductivities of B2-PdTi and B19-PdTi, B2-NiTi and B19'-NiTi are plotted together with the experimental curves of [40] for the two NiTi-phases. No measurements are available for PdTi. The calculated optical conductivities for the two PdTi phases show characteristic differences (figure 5, top). For B2-PdTi, a dominant peak at 0.9 eV is separated by a minimum at 1.5 eV from a broad peak from 1.8 to 4 eV showing some structure at 1.9, 2.2, 2.6, 3.0, 3.6 and 4.0 eV and a shoulder at 2.9 eV. For the B19 phase, the peak at 0.9 eV appears only as a shoulder, the minimum is shifted by 0.3 eV to 1.2 eV, and the broad peak now has only maxima at 2.2 and 2.7 eV with a steeper descent at the high-energy side and only a broad shoulder at 4 eV. These differences in the optical spectra can be ascribed to the symmetry splitting of many flat bands of B2-PdTi in the low-temperature phase.

The calculated optical conductivity of B2-NiTi shows peaks at 0.3, 1.0, 1.8, 2.1 and 3.8 eV and a shoulder at 3 eV with two minima at 0.6 and 3.3 eV. Experimentally, peaks are found at 0.3 eV (not shown in figure 5), 1.0, 2.1, 2.9 eV and a shoulder at 3.2 eV. There is no peak discernible in the measured spectrum near 4 eV, but a small shoulder can be seen at 1.8 eV. From the shape of the curves it is obvious, that a shift of the calculated curve by 0.3 eV to higher energy would certainly improve agreement with experiment.

Experimental and theoretical peak positions for B19'-NiTi agree very well. The peak found at 0.7 eV in both theory and experiment is not present in B2-NiTi. However, the calculated peak has a much lower relative intensity than experimentally found. As transition moments have been assumed to be constant, peak intensities are not reproduced reliably. After this peak, a minimum at 1.05 eV (1.2 eV in experiment) is followed by a broad peak extending from 1.8 to 3.5 eV. The calculated curve shows two maxima at 1.9 and 2.3 eV and shoulders at 3.2 and 3.8 eV, whereas experiment yields two maxima at 2.2 and 2.6 eV and a shoulder at 3.2 eV. Agreement with experiment is certainly much better than in [26].

Thus, even though excited states are not well defined in the density functional theory, the essential features of the optical conductivity calculation (a broad peak from 1.5 to 3.5 eV with only minor differences in structure for both compounds; an additional peak at 0.7 eV for the martensite and additional peaks at very low energies for B2-NiTi) are well reproduced in such a calculation. A proper treatment of transition moments would probably improve the relative peak intensities and peak positions could be shifted by a more sophisticated treatment of self-energy effects also for excited states (where the same approximate formula as for bound states was used, analogous to the calculation of the XPS spectra).
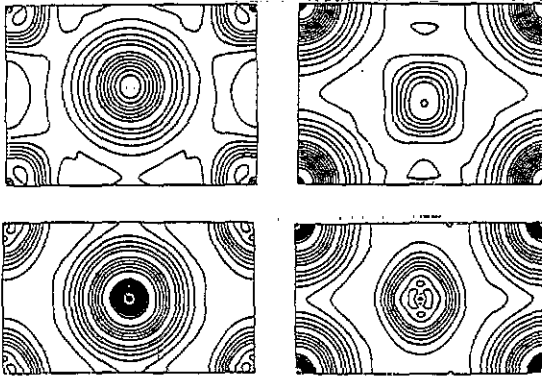
Figure 6. Contour plot of the valence electron density of B19'-NiTi (top) and B19-PdTi (bottom) in two planes corresponding to the $(1\bar{1}0)_{B2}$ plane of the B2 compounds with either the Ni(Pd) (left) or the Ti (right) atom in the centre and the other atom at the corners. A logarithmic mesh of distance $^4\sqrt{e}$ is used, starting with a density of $0.1e\,\text{Å}^{-3}$.

3.3. Electron densities

Figure 6 shows contour plots for the electron density of B19'-NiTi in the $(010)_{B19'}$ plane and of B19-PdTi in the $(100)_{B19}$ plane. These planes correspond to the $(1\bar{1}0)_{B2}$ plane, but for B19'-NiTi, the nearest-neighbour Ni and Ti atoms are not in-plane (see figure 1). Thus, two different cuts are shown with either the Ni or the Ti atom lying in-plane. The plots are to be compared with the (110) cuts of the electron density of B2-NiTi and B2-PdTi (figure 4 in [27]).

For B19'-NiTi some Ti–Ti bonding can be detected in the cut with the Ti atoms in-plane. The Ni electron density is spherically symmetric and there are no signs of Ni–Ti bonding. For B19-PdTi, no Pd–Ti bonding is found, either. The smaller Pd–Pd distance in the low-temperature phase causes an increased overlap of the spherical Pd electron densities, but no real Pd–Pd bonding. There are also no signs for Ti–Ti bonding. Compared to the electron densities of the B2-phases [27], there seems to be little influence of the phase transformation on the electron density.

3.4. Fermi surfaces

In order to facilitate the comparison of high- and low-temperature phase Fermi surfaces, we used a partly extended Brillouin zone scheme for the low-temperature phases. The doubling of the real-space unit cell for B19'-NiTi and B19-PdTi compared to the B2 phases corresponds to a bisection of the Brillouin zone. By partitioning the smaller Brillouin zone in four trigonal prisms (the left side of figure 7) and shifting them by a reciprocal lattice vector in the k_x, $-k_x$, k_z and $-k_z$ direction and by a distortion of the resulting double-sized Brillouin zone compensating the distortions in real space, an extended Brillouin zone (the right side of figure 7) of comparable size to the Brillouin zone of the cubic phases is obtained.
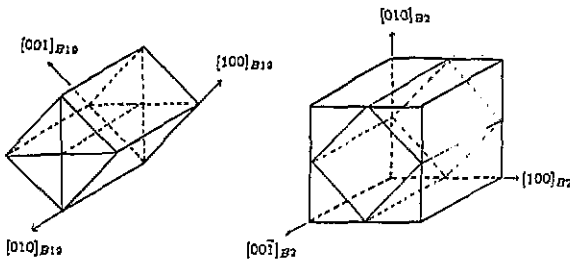

Figure 7. Brillouin zone of the martensitic (left) and austenitic phase (right) of PdTi and geometric unfolding of the Brillouin zone of the martensitic B19-PdTi phase.

Figure 8 shows the Fermi surface cuts for bands 14 and 16 of B19'-NiTi (*a*) and B19-PdTi (*b*) in the plane corresponding to the (100) plane of B2-NiTi and B2-PdTi. These cuts should be compared to Figure 6 of [27]. As in [27], the full curves correspond to the Fermi surface at 0 K or to all states at the martensitic transformation temperature with an occupation number of 0.5. Chain and broken curves characterize states with an occupation degree of 60–90% and 10–40%, respectively, thus taking into account the temperature smearing of the Fermi surface.
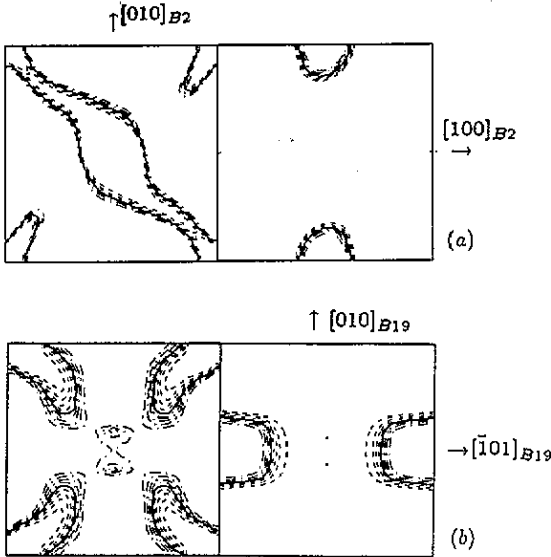
$\uparrow [010]_{B2}$

$[100]_{B2}$
$\rightarrow$

(*a*)

$\uparrow [010]_{B19}$

$\rightarrow [\bar{1}01]_{B19}$

(*b*)

Figure 8. Cut through the Fermi surfaces of B19'-NiTi (*a*) and B19-PdTi (*b*) corresponding to the (001) cuts of the B2 phases for band 14 (holes, left) and 16 (electrons, right). Full curves: half-occupied states at the martensitic transformation temperatures of 333 K (NiTi) and 840 K (PdTi). Broken curves: occupation 10–40%, chain curves: occupation 60–90%.

Compared to B2-NiTi, the lower symmetry of the monoclinic phase produces more asymmetric Fermi surface cuts. For the 14th band, two connected hole necks are found only in the [$\bar{1}$10] direction, whereas only small separate hole pockets remain in the [110] direction. Only two and much smaller electron pockets than for B2-NiTi can be detected for the 16th band.

For PdTi, the 14th band produces four rather asymmetric unconnected hole necks. Band 16 shows also only two electron pockets, however they are more extended than for B19'-NiTi.

Figure 9(*a*)–(*d*) shows the three-dimensional Fermi surfaces for the (13th plus 14th) and (15th plus 16th) bands of B19'-NiTi and B19-PdTi drawn for the extended Brillouin zone of figure 6. Some discontinuities are artefacts of the extended and slightly distorted Brillouin zone, but one recognizes easily the similarities with the comparable Fermi surface plots for the B2-phases of [27], especially between the plots for the (15th plus 16th) band of B19'-NiTi and the 8th band of B2-NiTi. As to the (13th plus 14th) band of B19'-NiTi, the hole surface is reduced compared to the Fermi surface for the 7th band of B2-NiTi and two separate hole sheets are formed. The same effect can also be detected in the Fermi surface for the (13th plus 14th) band of B19-PdTi. A superficial inspection of the Fermi surfaces of B19'-NiTi and B19-PdTi does not identify any obvious candidates for nesting hole and electron regions which would, however, be essential for an explanation of the phase transition martensite into austenite by the softening of particular branches of the phonon spectra, as was done for the reverse phase transition austenite into martensite, occurring on cooling B2-NiTi [27]. The transformation of martensite into austenite is less
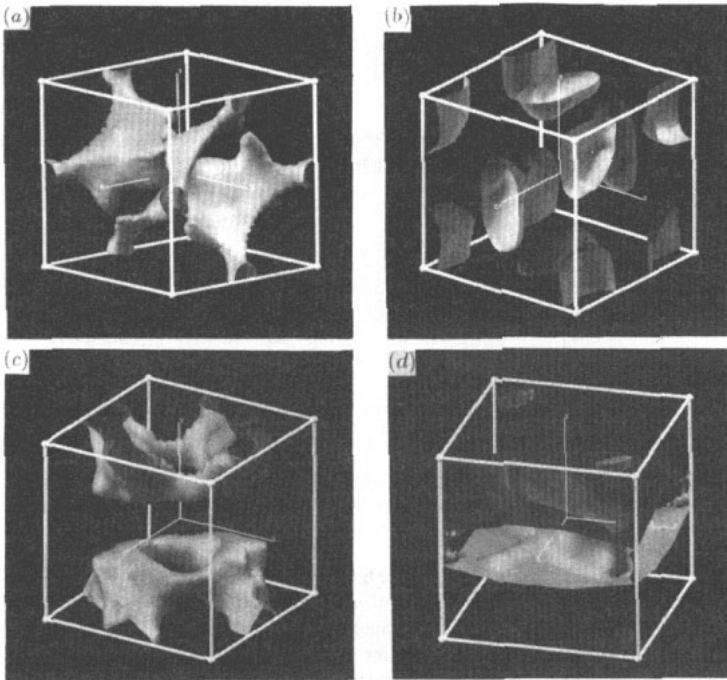
Figure 9. 3D Fermi surfaces of B19'-NiTi for bands 13 and 14 (*a*) and 15 and 16 (*b*), and of B19-PdTi for bands 13 and 14 (*c*) and 15 and 16 (*d*) in the 'unfolded' representation.

well investigated, experimentally, and one lacks information about the phonons involved in it. The reversal of the transformation austenite into martensite would correspond to nesting vectors $q = \frac{1}{3}[010]$ for B19'-NiTi and $q = \frac{1}{3}[100]$ for B19-PdTi going soft, but it is difficult to find such vectors in figures 8 and 9.

Analogous to [27], we can achieve a quantitative measure of the occurrence of nesting regions of the Fermi surface and of their importance for the softening of particular phonon branches by calculating the generalized susceptibility of non-interacting electrons $\chi_0(q)$ and the function $\zeta(q)$ [27] in several crystallographic directions.

3.5. Generalized susceptibility and electron–phonon coupling

In the model of Varma and Weber [42], the electron–phonon coupling contribution $D_2(q)$ of a phonon q to the dynamical matrix of phonons can be approximated by a function

$$\zeta(q) = \sum_{k,m,m'} (v^q_{k,m} - v^q_{k+q,m'})^2 \frac{f(E^m_k) - f(E^{m'}_{k+q})}{E^m_k - E^{m'}_{k+q}}$$

where

$$v^q_{k,m} = (\partial E^m_k / \partial k)^q$$

is the energy gradient in the direction of q.

The most significant contributions can be expected from the bands near the Fermi level. For a phonon q_1 going soft, the function $\zeta(q)$ must have a maximum at $q = q_1$. For this purpose, there must be nesting regions in the Fermi surface which are connected by q_1 and produce a maximum in the generalized susceptibility of non-interacting electrons

$$\chi_0(q) = \sum_{k,m,m'} \frac{f(E^m_k) - f(E^{m'}_{k+q})}{E^m_k - E^{m'}_{k+q}}$$

which can be regarded as an approximation for $\zeta(q)$ neglecting the influence of energy gradients. The second condition for a maximum of $\zeta(q)$ is a saddle point of the Fermi surface in direction of the vector q_l connecting the nesting hole and electron Fermi surface regions.

To illustrate the differences between $\chi(q)$ and $\zeta(q)$ we calculated both functions for a Fehlner and Lolly Fermi surface [43], where the energy dispersion law is taken to be

$$\epsilon(k) = \frac{|k|^2 + R \max(|k_x|, |k_y|, |k_z|)}{1 + R}$$

which should produce a nesting vector at $|2k_f|$, provided R is large enough (for $R \to 0$ the free-electron Fermi sphere is obtained, whereas a large R gives a more cube-like shape with 'sides' of length $|2k_f|$). We see in figure 10, that the generalized susceptibility exhibits a peak superimposed on the free-electron 'background' (Linhard function), $\chi(|2k_f|)$ being of the same order of magnitude as $\chi(0)$. In contrast, only q vectors around $|2k_f|$ make significant contributions to $\zeta(q)$, thus producing a much more significant peak without 'background'. This should justify the use of $\zeta(q)$ for a quick screening of the Fermi surface to find possible phonon anomalies.
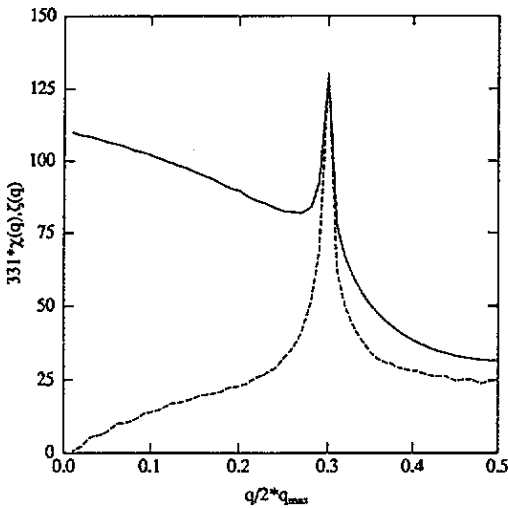

Figure 10. Generalized susceptibility $\chi_0(q)$ and function $\zeta(q)$ (broken) for a Fehlner and Lolly Fermi surface with $R = 8$ and $k_f = 0.15$.

In figure 11, we have plotted the generalized susceptibilities for B19'-NiTi (full curve) and B19-PdTi (broken curve) for the $[111]_{B19,B19'}$ (*a*), the $[010]_{B19}$ ($[100]_{B19'}$) (*b*) and the $[001]_{B19,B19'}$ direction (*c*). The eight [111], two [001] and two [010] ([100]) directions of the martensitic phases correspond to the twelve (equivalent) [110] directions in the austenitic phases (cf. figure 7). In all susceptibility calculations the sums over m and m' are extended only over bands crossing the Fermi surface.

For B19'-NiTi, no nesting is found in the [111] or [010] direction except for a small peak at $[0.2, 0.2, 0.2]2\pi/a$. $\chi_0(q)$ has only a maximum in the [001] direction near $q = q_{max}$, which is shifted for B19-PdTi to $[0, 0, 0.38]2\pi/a$. The susceptibility of B19-PdTi has also a maximum in the [111] direction for $q = [0.28, 0.28, 0.28]2\pi/a$.

Inspection of the $\zeta(q)$ curves for the [111], [001], and [010] ([100]) directions (figure 12) shows that for the two martensitic phases no maxima appear in the [001] or [100] ([010]) direction, but there are distinct maxima in the [111] direction for B19'-NiTi at $[0.19, 0.19, 0.19]2\pi/a$ and for B19-PdTi at $[0.3, 0.3, 0.3]2\pi/a$. Thus, softening of
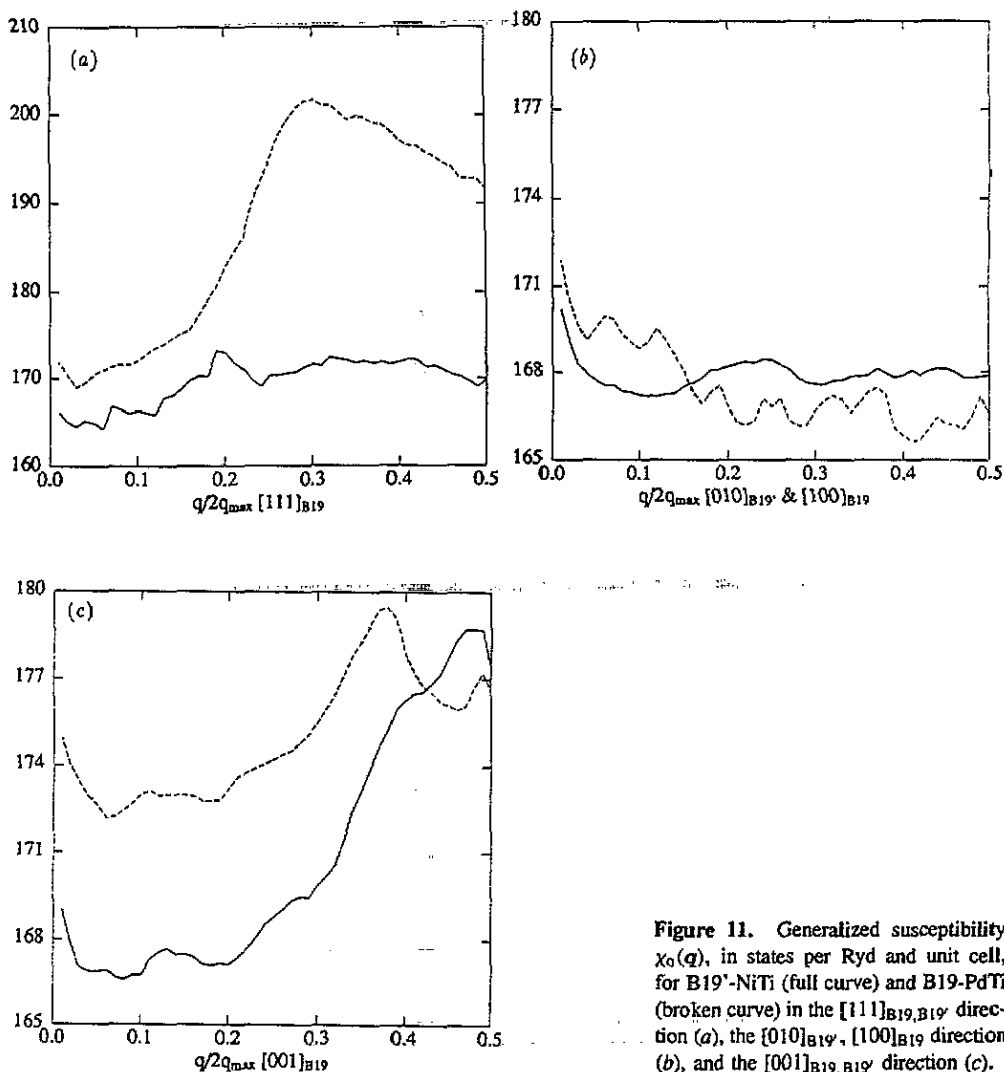
Figure 11. Generalized susceptibility $\chi_0(q)$, in states per Ryd and unit cell, for B19'-NiTi (full curve) and B19-PdTi (broken curve) in the $[111]_{B19,B19'}$ direction (a), the $[010]_{B19'}$, $[100]_{B19}$ direction (b), and the $[001]_{B19,B19'}$ direction (c).

phonons can only be expected in the [111] direction and not in the [100] ([010]) direction corresponding to those [110] directions of the B2 phases, where phonon softening initiates the transformation from austenite into martensite. A simple reversal of this transformation mechanism for the reverse transformation martensite into austenite is therefore not very probable.

From figures 11 and 12, the martensitic phases have much less possibilities of phonons going soft and should therefore be much harder compared to the austenitic phases as is indeed found by experiment [5].

4. Conclusion

The LAPW band structure calculations for B19'-NiTi and B19-PdTi furnish XPS spectra and optical conductivities in good agreement with experiment if available; however, self-energy corrections are necessary for the NiTi phases. Measurements of the optical conductivities of
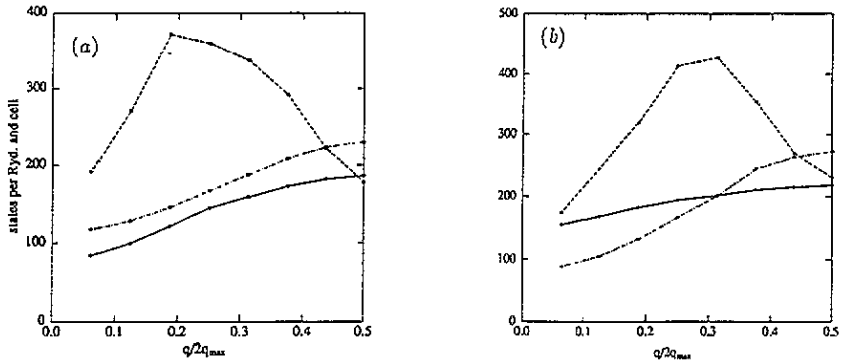
Figure 12. $\zeta(q)$ (in states per Ryd and unit cell) for B19'-NiTi (*a*) and B19-PdTi (*b*). Broken curve: [111] direction; full curve: $[010]_{B19'}$ or $[100]_{B19}$ direction; chain curve: [001] direction.

B2-PdTi and B19-PdTi and new measurements of the XPS spectra of B2-PdTi and B19'-NiTi would be desirable.

The general shape of the DOS and bandwidths do not change much at the phase transition. Due to the reduced symmetry of the martensitic phases, energy bands are split and the DOS peaks are lower and more structured. The d electrons are more localized in the martensitic phases. The DOS at the Fermi level is 20% lower for them, indicating a higher stability of the martensitic than of the austenitic phases at lower temperatures. A quantitative discussion of the relative stabilities of both NiTi and PdTi phases must be postponed to a further paper [29].

Electron densities are also very similar for both phases. The Fermi surfaces change, though, at the phase transition. In particular, the characteristic nesting features between hole and electron energy surfaces have almost disappeared, which is best seen from the plots of the generalized susceptibility $\chi_0(q)$ and of the function $\zeta(q)$ ($\zeta(q)$ shows only maxima in the [111] direction and not in the other symmetry directions which are equivalent in the B2 phases, i.e. the $[110]_{B2}$ directions). Thus, the possibility of phonons going soft as a first step of the martensitic phase transition is reduced and the martensitic phases should be harder than the B2 phases as is indeed the case. It would be very interesting to compare experimental investigations of the phase transition martensite into austenite of NiTi and PdTi to the several existing investigations for the reverse transformation austenite into martensite.

Acknowledgments

References

[1] Michal G M and Sinclair R 1981 *Acta Cryst.* B **37** 1803
[2] Wang F E, Buehler W J and Pickart S J 1965 *J. Appl. Phys.* **36** 3232
[3] Ossi P M and Rossitto F 1981 *J. Phys. F: Met. Phys.* **11** 2037
    Wasilewski R J 1975 *Shape Memory Effects in Alloys* ed. J Perkins (New York: Plenum) pp 245–71

[4]   Pushin V G, Kondrat'ev V V and Khachin V N 1985 *Sov. Phys. J.* **28** 341
[5]   Herget G, Müllner M, Suck J B, Schmidt R and Wipf H 1989 *Europhys. Lett.* **10** 49
[6]   Zhao X, Wu X and Ko T 1989 *Acta Met.* **37** 1783
[7]   Dwight A E, Conner R A Jr and Downey J W 1965 *Acta Cryst.* **18** 835
[8]   Raub E and Röschel E 1968 *Z. Metallkunde* **59** 112
[9]   Shabalovskaya S A, Lotkov A I, Narmonev A G and Zakharov A I 1987 *Solid State Commun.* **62** 93
[10] Mitchell M A, Wang F E and Cullen J R 1974 *J. Appl. Phys.* **45** 3337
[11] Egorushkin V E and Kulkova S E 1982 *J. Phys. F: Met. Phys.* **12** 2823
[12] Egorushkin V E, Kul'ment'yev A I and Flat A Ya 1987 *J. Phys. F: Met. Phys.* **17** 289
[13] Shabalovskaya S A 1985 *Phys. Stat. Sol (b)* **132** 327
[14] Papaconstantopoulos D A, Kamm G N and Poulopoulos P N 1982 *Solid State Commun.* **41** 93
[15] Savushkin E, Lapin V B and Egorushkin V E 1991 *J. Phys.: Condens. Matter* **3** 9185
[16] Zhao G-L, Leung T C, Harmon B N, Keil M, Müllner M and Weber W 1989 *Phys. Rev. B* **40** 7999
[17] Miller M L, Antonov V N, Zhalko-Titarenko A V, Plotnikov N A and Nemoshkalenko V V 1988 *Sov. Phys. Doklady* **33** 835
[18] Hwang C M, Meichele M, Salamon M B and Wayman C M 1983 *Phil. Mag.* **47** 9
[19] Boletskaya T K, Egorushkin V E, Savitskii E M and Fadin V P 1980 *Sov. Phys. Doklady* **252** 87
[20] Egorushkin V E 1982 *Sov. Phys. Solid State* **24** 725
[21] Bruinsma R 1982 *Phys. Rev. B* **25** 2951
[22] Shore J D and Papaconstantopoulos D A 1984 *J. Phys. Chem. Sol.* **45** 439
[23] Eibler R, Redinger J and Neckel A 1987 *J. Phys. F: Met. Phys.* **17** 1533
[24] Lapin V B, Egorushkin V E, Shabalovskaya S A and Ivanova O P 1990 *Solid State Commun.* **73** 471
[25] Naumov I I, Velikokhatnyi D I and Bashirov V Z 1991 *Pis'ma Zh. Eksp. Teor. Fiz.* **54** 571
[26] Kulkova S E, Egorushkin V E and Kalchikhin V V 1991 *Solid State Commun.* **77** 667
[27] Bihlmayer G, Eibler R and Neckel A 1992 *Ber. Bunsenges. Phys. Chemie* **96** 1626
[28] Enami K, Yoshida T and Nemo S 1986 *Proc. Int. Conf. Mart. Transformations (ICOMAT 86), Nara (Japan)*
[29] Bihlmayer G, Eibler R and Neckel A 1993 in preparation
[30] Koelling D D and Arbman G O 1975 *J. Phys. F: Met. Phys.* **5** 2041
      Andersen O K 1975 *Phys. Rev. B* **12** 3060
[31] Hedin L and Lundqvist B I 1971 *J. Phys. C: Solid State Phys.* **4** 2064
[32] Donkersloot H C and van Vucht J H N 1970 *J. Less Common Met.* **20** 83
[33] Bradley C J and Cracknell A P 1972 *The Mathematical Theory of Symmetry in Solids* (Oxford: Oxford University Press)
[34] Kittel C and Fong C Y 1988 *Quantum Thoeory of Solids* (New York: Wiley)
[35] Lehmann G and Taut M 1972 *Phys. Stat. Sol.* **54** 469
[36] Shabalovskaya S A, Lotkov A I, Sasovskaya I I, Narmonev A G and Zakharov A I 1979 *Solid State Commun.* **32** 735
[37] Redinger J, Marksteiner P and Weinberger P 1986 *Z. Phys. B* **63** 321
[38] Davis C C 1986 *J. Appl. Phys.* **59** R25
[39] Lashkarev G V, Solonin S M, Brodovoĭ A V, Martynova I F, Radchenko M V, Mirets A L and Goncharuk N V 1992 *Sov. Phys. Solid State* **34** 352
[40] Sasovskaya I I, Shabalovskaya S A and Lotkov A I 1979 *Sov. Phys.–JETP* **50** 1128
[41] Koelling D D, Mueller F M and Veal B W 1974 *Phys. Rev. B* **10** 1290
[42] Varma C M and Weber W 1979 *Phys. Rev. B* **19** 6142
[43] Fehlner W R and Lolly P D 1974 *Solid State Commun.* **14** 653